Extended abstracts from the SME journal Mining, Metallurgy & Exploration

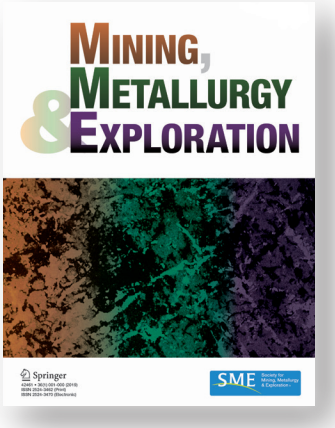

Take full advantage of your SME membership. As a member, you can read and download for free all of the full-text papers in *Mining, Metallurgy & Exploration* (**MME**) and the archives of *Minerals & Metallurgical Processing* (**MMP**). Log in to the SME website as a member, and enter the MME Springer website through our dedicated SME link:

1. Log in at smenet.org with your email address and password.
2. Click on "Publications" in the top banner and choose "Mining, Metallurgy & Exploration journal" in the pull-down menu.
3. Scroll down and click on the "Read the MME Journal Online" link. This takes you to the MME Springer website as an SME member with free access.

To see a specific paper, use the search function or use the paper's https://doi link.

For assistance at any time, email Chee Theng at theng@smenet.org. ■

Optimal pitwall shapes to increase financial return and decrease carbon footprint of openpit mines

S. Utili[1,2,*], A. Agosti[2], N. Morales[3], C. Valderrama[4], R. Pell[5] and G. Albornoz[6]

[1]OptimalSlope Ltd, London, UK
[2]School of Engineering, Newcastle University, Newcastle upon Tyne, UK
[3]Département de Génies Civil Géologique et des Mines, Polytechnique Montréal, Canada
[4]Itasca Chile, Santiago, Chile
[5]Minviro Ltd, London, UK
[6]SRK Chile, Santiago, Chile
*Corresponding author email: stefano_utili@optimalslope.com

Full-text paper:
Mining, Metallurgy & Exploration (2022) 39:335–355, https://doi.org/10.1007/s42461-022-00546-8

Keywords: Optimal pitwalls, NPV optimization, Carbon footprint reduction

Special Extended Abstract

The steepness of an openpit mine's slopes has a substantial influence on the mine's financial return. This paper proposes a novel design methodology where overall steeper pitwalls are employed without compromising the safety of the mine. In current design practice, pitwall profiles are often planar in cross section within each rock layer: that is, the profile inclination across each layer tends to be constant. Here, instead, a new geotechnical software, OptimalSlope, is used to determine optimal pitwall profiles of depth-varying inclination. OptimalSlope seeks the solution of a mathematical optimization problem where the overall steepness of the pitwall, from crest to toe, is maximized for an assigned lithology, geotechnical properties and factor of safety (FoS). Bench geometries — bench height, face inclination, minimum berm width — are imposed in the optimization as constraints that bind the maximum local inclination of the sought optimal profile together with any other constraints, such as geological discontinuities, that may influence slope failure. The obtained optimal profiles are always steeper than their planar counterparts — that is, the planar profiles exhibiting the same FoS — up to 8 degrees, depending on rock type and severity of constraints on local inclinations. The design of a copper mine is first carried out with planar pitwalls, and then adopting the optimal pitwall profiles determined by OptimalSlope. The adoption of

optimal slope profiles leads to a 34 percent higher net present value (NPV), and reductions of carbon footprint and energy consumption of 0.17 Mt of carbon dioxide equivalent (CO_2 eq) and 82.5 million MJ, respectively, due to a 15 percent reduction of rockwaste volume.

Methodology

The block model of the copper deposit used as a case study was provided by a mining company collaborating with the Delphos Mine Planning Laboratory at the University of Chile. All the parameters needed to perform the pit design were taken from Parra et al. [1]. From the site lithology and geotechnical properties, two roughly uniform pit sectors were identified in Parra et al. [1]. In each sector, one representative cross section was assumed to design the pitwall profile. Table 1 lists the rock geotechnical parameters, and Table 2 the values adopted for the economic parameters and metallurgical recovery.

Pitwall design. In the design of pitwalls, we followed the standard practice of starting with the design of benches and then moved to the overall pitwall profiles. The height of the benches adopted for the whole mine was 10 m [1]. We computed the minimum berm width, b_w, using the modified Ritchie's criteria.

Then, we computed the geotechnically optimal slope profiles for the cross sections of the mine using the proprietary OptimalSlope code [2]. The code requires bench height, bench face inclination, minimum berm width and road width as inputs. The optimal pitwall profile is defined as the overall steepest safe profile: OSA = OSA_{max}, with OSA being the inclination over the horizontal of the line joining the pitwall toe to the crest (Fig. 1). OSA_{max} is determined by OptimalSlope iteratively. The main algorithm finds the optimal pitwall shape for an assigned OSA and geometric constraints ($\alpha_{i\,max}$ values). An initial-guess OSA value is first determined for the specified pitwall height, the geotechnical properties of all the layers and the specified FoS on the basis of a database of stability charts built in OptimalSlope. The FoS_i associated with the optimal profile found at the *i*-th iteration is then compared with the target FoS. If it is higher than the FoS_{target}, a steeper OSA is prescribed at the next iteration; if it is lower, a less steep OSA is prescribed.

Pit optimization. To assign the pitwall profiles into the Geovia Whittle pit optimizer, we split the block model into "zones" (according to the Whittle terminology) using Geovia Surpac and assigned a slope inclination to each zone. Then, to compute the ultimate pit limit (UPL) and pushbacks, we first ran Whittle to produce the discounted best-case-scenario curve in the pit-by-pit graph and then used the Milawa NPV algorithm to generate a specified-case-scenario curve for an initial set of pushbacks, chosen in correspondence of sharp increases exhibited by the best-case-scenario curve. Finally, we chose the UPL in correspondence to the highest point of the plateau exhibited by the specified-case curve.

Results

The pitwall profiles obtained as a result of the pit design process are plotted in Fig. 2a for pit sector 1. The FoSs of all the pitwall profiles were verified by performing a limit equilibrium method (LEM) analysis with the Morgenstern–Price method in Slide2 software. The pitwall profiles used in the Slide2 analyses are shown in Fig. 2b for the pit design adopting planar profiles and in Fig. 2c for the pit design adopting optimal profiles together with their FoSs. In all the cases, the FoS found is less than 1 percent from the target value of 1.3. For the optimal pitwall profiles, we performed additional stability analyses using the FLAC3D 7.0 software, having assigned a unit length in the out-of-plane direction. The critical failure mechanisms identified by Slide2 and FLAC3D and the associated FoSs are shown in Fig. 2c. In both mine sec-

Table 1 – Geotechnical properties [1].

	UCS (MPa)	GSI	m_i	D	γ (kN/m³)
Pit sector S1	65	45	15	1	25.9
Pit sector S2	50	45	12	1	25.9

Table 2 – Economic parameters and metallurgical recovery [1].

Copper price	US$6,000/t	US$3/lb
Selling cost	US$1,700/t	US$0.85/lb
Reference mining cost (US$/t)	3.4	
Processing cost (US$/t)	6.1	
Metallurgical recovery (%)	85	
MCAF (US$/t/bench)	0.13	
Discount rate (%)	10	
Processing method limit (Mt/y)	5	
Mining limit (Mt/y)	10	

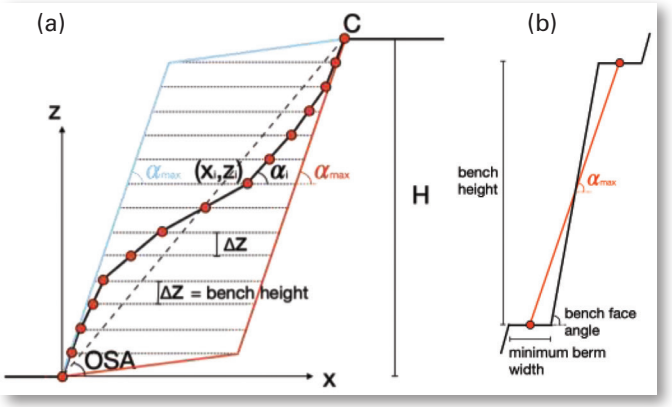

Fig. 1 (a) A generic candidate slope profile. The toe of the profile is at the origin (x_0, y_0), point C is the slope crest. A uniform discretization along the z direction is adopted. The red and blue lines enclose the region where the profiles are sought. The profile is discretized in n Δz intervals so there are $n - 1$ unknowns to be determined: $x_1, x_2, \ldots, x_{n-1}$. In the context of openpit mines, a good choice of Δz is to assume Δz equal to the bench height. (b) Determination of $\alpha_{i\,max}$ based on bench geometry (input to OptimalSlope).

Table 3 — Pit optimization economic and metallurgical results.

UPL output	Planar pitwalls		Optimal pitwalls	
	S1	S2	S1	S2
Overall slope angle (°)	48	43.8	50.1	51.3
H_{UPL} (m)	270	220	280	150
Waste (t)	23,707,500		20,651,462	
Ore (t)	59,314,446		59,232,285	
Stripping ratio	0.40		0.35	
NPV (US$)	34,561,747		46,231,284	
IRR (%)	13.9		15.8	
Life (year)	12.22		12.12	
Payback (year)	3.89		3.57	
NPV increase (%)	33.8			

tors, the FoSs found are less than 1 percent from the target value of 1.30.

Figure 2a allows a visual comparison between the planar pitwall profile of a traditional design, demarcated by the orange line, and the optimal pitwall profile, demarcated by the blue line. The optimal profile is clearly steeper than the planar one. The FoS of the entire UPL was verified by performing a 3D finite difference method analysis with FLAC3D 7.0. Throughout the entire mine, the minimum FoS found was 1.67. This value is significantly higher than the FoS values obtained earlier by the 2D FLAC analyses of approximately 1.30 and 1.31, respectively.

The key output data for the two design cases are provided in Table 3. The NPV for the design based on optimal pitwalls is around US$12 million higher than the NPV of the design based on planar pitwalls. Therefore, adoption of the optimal profiles would lead to a NPV increase of 34 percent. Such an increase is to be ascribed to a substantial decrease of rockwaste volume — around 15 percent, from 23.7×10^6 t to 20.7×10^6 t — while the amount of ore extracted is similar.

We computed the energy required to mine both orebody and waste rock together with the associated carbon footprint for both design types (with planar and with optimal pitwalls) based on Munoz et al. [3]. The energy consumption was calculated for each mined block of the UPL. The adoption of optimal pitwalls leads to reductions of carbon footprint and energy consumption of 0.17 Mt CO_2 eq and 82.5 million MJ, respectively, over the life of the mine. To provide some context, a reduction of 0.17 Mt CO_2 eq is equivalent to the carbon sequestered by 2.8 million tree seedlings grown for 10 years.

Conclusions

For the mine case study considered, the adoption of geotechnically optimal profiles led to a 34 percent higher NPV and reductions of carbon footprint and energy consumption of 0.17 Mt CO_2 eq and 82.5 million MJ, respectively, due to a 15 percent reduction of waste rock volume compared with the traditional design based on planar pitwalls.

The FoS values of the pitwall profiles determined by OptimalSlope were independently verified by two widely used geotechnical software packages for the geotechnical verification of openpit mines, Slide2 and FLAC, confirming that the pitwall profiles determined by OptimalSlope are as safe as their planar counterparts.

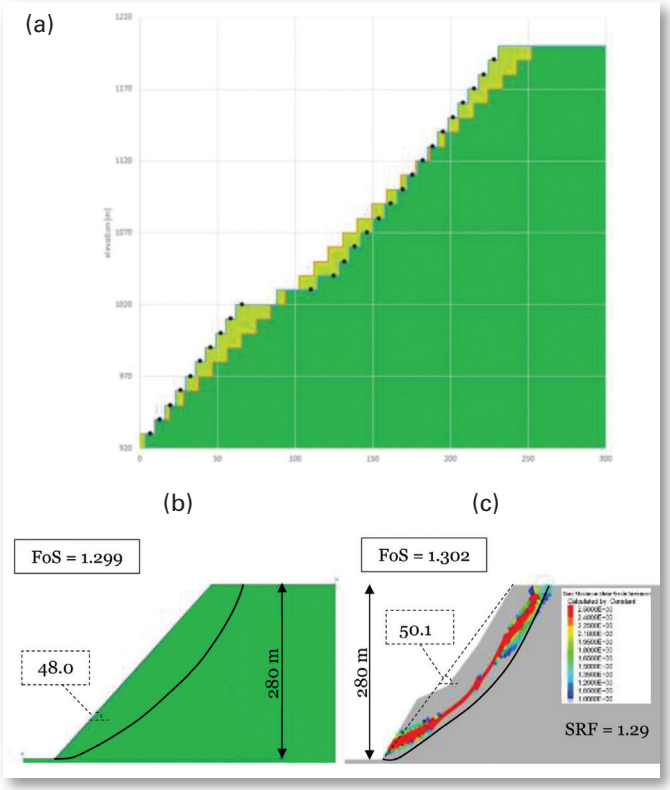

Fig. 2 UPL pitwalls for sector S1: (a) Comparison between the pitwall profile for traditional design (planar pitwall is in orange) and the optimal design (optimal pitwall is in blue, the black dots represent the x_i, z_i coordinates obtained as output from OptimalSlope. (b) Failure mechanism (black line) and FoS determined by 2D limit equilibrium method (Slide2) for the planar profile. (c) Failure mechanism (black line) and FoS determined by 2D limit equilibrium method (Slide2) and shear strain magnitude determined by finite difference method with shear strength reduction (FLAC3D) for the optimal profile.

OptimalSlope was also used in the designs of two other case studies: a contemporary mine being developed by Kinross [4], and the case of the McLaughlin mine, where a publicly available block model was used [5]. In both cases, employing optimal pitwall profiles in the mine design led to significant NPV increases, up to 52.7 percent, and substantial decreases of energy consumption and carbon footprint. ■

Selected references

1. Parra A, Morales N, Vallejos J, Nguyen PMV (2017) Openpit mine planning considering geomechanical fundamentals. Int J Min Reclam Environ 32(4):221–238
2. OptimalSlope (2021): Software for the determination of optimal profiles for slopes and pitwalls, www.optimalslope.com
3. Munoz J, Guzman RR, Botin JA (2014). Development of a methodology that integrates environmental and social attributes in the ore resource evaluation and mine planning. Int J Mining Mineral Eng 5:38–58
4. Agosti A, Utili S, Gregory D, Lapworth A, Samardzic J, Prawasono A (2021) Design of an openpit goldmine by optimal pitwall profiles. CIM Journal 12(4):149–168
5. Agosti A, Utili S, Valderrama C, Albornoz G (2021) Optimal pitwall profiles to maximise the overall slope angle of openpit mines: the McLaughlin mine. ACG Proceedings of Slope Stability in Mining Conference, Perth, Australia, 69–82

MME Technical-Paper Abstracts

Electromagnetic interference (EMI) in underground coal mines: A literature review and practical considerations

Chenming Zhou*, Miguel Reyes and Matthew Girman
CDC NIOSH, Pittsburgh, PA, USA
*Corresponding author email: czhou@cdc.gov

Full-text paper:
Mining, Metallurgy & Exploration (2022) 39:421–431, https://doi.org/10.1007/s42461-021-00535-3

Keywords: Electromagnetic interference (EMI), Electromagnetic compatibility (EMC), Radio emission

Special Extended Abstract

This paper is aimed at helping the mining industry to better understand the challenges posed by electromagnetic interference (EMI) and to promote electromagnetic compatibility (EMC) in underground coal mines. The paper begins with a review of EMI standards in other industries, then presents some representative examples of EMI instances that have occurred in the mining industry, followed by a literature review of published EMI research in mining and, finally, a discussion on mitigation strategies and practical considerations related to EMI in mining.

Introduction

Modern smart mining increasingly depends on the use of sophisticated electrical and electronic systems for improved safety and better productivity. With more electronic systems being introduced underground, the mining industry is facing electromagnetic compatibility (EMC) issues caused by electromagnetic energy emitted by one device adversely impacting the normal function of another.

As shown in the EMI triangle model in Fig. 1, an EMI instance is usually associated with three key components: a source, a victim, and coupling/propagation paths from the source to the victim. All three elements in underground mining environments are unique as compared to those elements in other environments, and thus, the EMI in underground mining deserves a special consideration.

EMI instances, scope and standards

Historically, there have been a variety of EMI instances reported in underground coal mines. One of the most recent notable EMI instances is that the magnetic fields emitted from a personal dust monitor interfere with the normal operation of a proximity detection system. More examples can be found in the full paper.

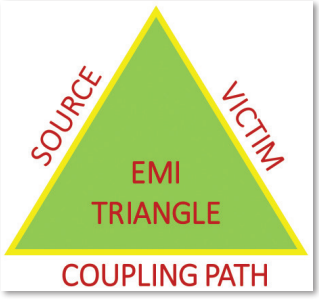

Fig. 1 An EMI triangle model to illustrate the three key elements for an EMI instance to occur.

EMI standards have been formulated to ensure that electronic devices and systems are able to tolerate a specified degree of interference and not generate more than a specified amount of interference. As a result, the scope of EMI typically includes two broad categories: susceptibility and emissions. The susceptibility category includes characterizing a victim's susceptibility to conducted emissions, radiated emissions, lightning and electrostatic discharge (ESD), and comparing them to the corresponding given regulatory limits. The emissions category then covers characterizing and regulating conducted and radiated emissions from a device across the spectrum.

Currently, a standard or set of requirements for dealing with EMI specifically in mining does not exist. However, numerous organizations have attempted to resolve EMI issues by developing standards for emissions and susceptibility testing in other industries. For example, in the United States, the U.S. military created the standard MIL-STD-461 to control the EMI issues in subsystems and equipment used in military environments. A review of EMI standards developed in other industries that may be applicable to mining can be found in Girman et al. [1].

Published research, mitigation strategies and practical considerations

Although it has been extensively investigated in many other industries, EMI in the mining industry has received much less attention, and the corresponding published research pertaining to EMI in mining is relatively scarce. Some major research efforts conducted by different institutions in the world are reviewed in the full paper.

Generally, EMI effects can be mitigated by attacking one or more of the three elements shown in Fig. 1. Particularly, EMI mitigation can be achieved by (1) suppressing the emission at its source, (2) making the coupling path less efficient, and (3) making the victim more robust to the emission. Typical EMI mitigation strategies include shielding, grounding, filtering and distancing, which are discussed in detail in the full paper.

Mineworkers should consider the EMI triangle — that is, source, victim and path — when examining a suspected EMI incident and stay alert when operating electronic devices in the vicinity of EMI sources. Some practical examples of potential EMI sources in an underground coal mine are wireless communication and tracking systems, such as handheld radios; electronic systems, such as personal dust monitors, called PDMs; power centers; variable-frequency-drive systems; electric motors; and lightning, whose effects can penetrate the earth overburden and reach areas inside a mine.

In addition to the mitigation strategies discussed above, EMI effects and associated safety concerns can be ultimately

reduced by developing and applying EMI standards across the mining industry. The formulations of EMI standards often are related to the equipment and operational environments in a specific industry. As such, different EMI standards are formulated for different industries. Compared to other industries, the mining industry has some unique characteristics in terms of its geological and EM environments that one must consider when developing a mining-specific EMI standard.

Conclusions

An overview of EMI in underground coal mines is presented, and the impacts and practical solutions of EMI that can affect the health and safety of mineworkers are investigated. Some key issues and practical considerations pertaining to EMI in mining are highlighted. It is concluded that similar to EMI standards that were developed in many other industries decades ago, ultimately mining-specific EMI standards may need to be promoted to overcome the increasing EMI issues in underground mining. ■

Selected reference

1. Girman M, Reyes M, Zhou C (2022) An overview of existing EMI standards applicable to mining. Mining Metall Explor 39(1):77–88

Trace-element content and partition in apatite-group minerals in phosphate ore from Catalão, Brazil

Angela Nair Avelar[1,*], Paulo R.G. Brandão[1] and Reiner Neumann[2]

[1]Department of Mining Engineering, Federal University of Minas Gerais, Belo Horizonte, Brazil

[2]Centre for Mineral Technology, Division for Technological Characterisation, Rio de Janeiro, Brazil, and Postgraduate Program in Geosciences, National Museum, Federal University of Rio de Janeiro, Rio de Janeiro, Brazil

*Corresponding author email: angelaavelar@gmail.com

Full-text paper:
Mining, Metallurgy & Exploration (2022) 39:679–688, https://doi.org/10.1007/s42461-022-00559-3

Keywords: Apatite, Phosphate ore, LA-ICP-MS, Electron microprobe, Trace elements, Compositional zoning

Special Extended Abstract

Three types of apatite were identified by means of cathodoluminescence (CL) images in flotation concentrate and tailing samples from the Catalão Mine in Brazil. They are predominantly blue apatite, followed by green apatite and, less frequently, yellow apatite. The chemical compositions of these types of apatite were determined by electron microprobe analysis and laser ablation-inductively coupled plasma-mass spectrometry (LA-ICP-MS). Blue and green apatite responded well to the process, thus remaining in the concentrate, while yellow apatite remained in the tailings. Yellow apatite has the lowest phosphorus pentoxide (P_2O_5) content and largest anionic and cationic sites substitution, followed by green apatite, whereas blue apatite is the most homogeneous, with highest phosphorus (P) and calcium (Ca) grades and lowest substitution level. A negative correlation of the amount of phosphorus with fluorine was observed. Furthermore, impregnation of iron oxide-hydroxides in the yellow apatite was also observed. Therefore, the low flotation behavior is due to low crystallinity coupled with impregnation onto its surface.

Background

Phosphorus is obtained from the mining of phosphate rocks — mainly, the mining of minerals belonging to the apatite group. These ores represent a limited and nonrenewable resource [1]. Apatite supergroup is a term referring to a series of hexagonal and monoclinic phosphates having the general chemical formula $^{IX}M1_4{}^{VII}M2_6(^{IV}TO_4)_6X_2$ [2]. The most common minerals of this group are the calcium phosphates, and the occupation of the X site defines terms as fluorapatite, chlorapatite or hydroxylapatite, while Ca occupies both the M1 and M2 sites. Although the predominance in the occupation of the sites defines the mineral name, its composition may be more complex.

The flotation efficiency of phosphate ores of igneous origin is influenced by the mineralogical composition of the ore that feeds the concentration process. Several studies tried to link the chemical composition of apatite to process efficiency, but usually no significant differences could be detected in the bulk sample.

In this study, based on CL analyses, we attempt to establish a correlation between the CL color and the chemi-

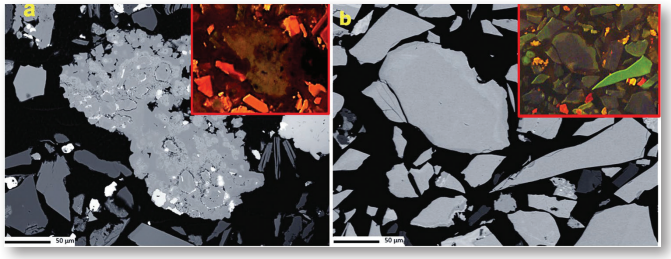

Fig. 1 BSE images of apatite from siliceous carbonate ore by electron microprobe analysis, and their respective CL images (inserts) of the different colors of the apatite: (a) extensively altered texture, typical of yellow apatite, and (b) green apatite as a rim of blue apatite and liberated green apatite. Carbonates are colored yellow/orange (calcite) and red/pink (dolomite).

cal composition of the different types of apatite from the Catalão Mine in Brazil. Variations in composition and zoning were found in apatite grains in the concentrate and waste from flotation.

The LA-ICP-MS data complement the quantification of the elements, which were identified by electron microprobe analysis for the separate apatite types. The results of these analyses are useful to guide the development of process routes that may contribute to increase the flotation performance.

Results

The CL images identified three types of apatite: blue apatite, green apatite and yellow apatite. Apatite with blue and green hues under CL are dominant in the concentrates, while yellow and green apatite are common in tailings. Compositional zoning is common and detectable in optical-microscope and backscattered-electron (BSE) images. There are a considerable number of grains with a blue apatite core and green apatite rim (Fig. 1).

The correlation of CL colors and processing performance is established for the first time in this study, and the chemical signature accounting for the CL colors could potentially also have an impact on the processing performance.

Electron-microprobe and LA-ICP-MS point analysis were performed on these blue, green and yellow domains of apatite in order to reveal compositional contrasts. Table 1 presents the average compositions and standard deviations of the blue, green and yellow apatite. The structural formula was calculated based on 10 M-site atom occupancy. According to wavelength dispersive spectrometry analysis, all the types of apatite investigated in this study are fluorapatite, bearing more than 2 percent fluorine (F) by mass with the chlorine (Cl) content either at the limit or below electron-microprobe detection.

Table 1 — Chemical composition (electron microprobe analysis) and calculation of the structural formula (based on 10 M-site atom occupancy) of the types of apatite differentiated by CL (N = number of analyses for each type).

	Oxides (wt %)	Blue apatite (N=129)		Green apatite (N=95)		Yellow apatite (N=62)	
		avg	StDev	avg	StDev	avg	StDev
	CaO	52.15	0.78	49.89	2.42	49.82	2.47
	Na_2O	0.1	0.10	0.18	0.13	0.44	0.69
	SrO	0.79	0.24	2.93	2.58	1.77	1.53
	MnO	0.01	0.01	0.08	0.11	0.05	0.06
	Fe_2O_3	0.03	0.03	0.07	0.09	0.21	0.43
	MgO	0.03	0.08	0.25	0.39	0.36	0.59
	La_2O_3	0.24	0.14	0.19	0.17	0.15	0.14
	Ce_2O_3	0.57	0.30	0.58	0.41	0.55	0.35
	Pr_2O_3	0.08	0.22	0.06	0.05	0.06	0.06
	Nd_2O_3	0.22	0.16	0.21	0.19	0.06	0.21
	P_2O_5	40.61	0.60	38.01	2.68	37.02	3.49
	SiO_2	0.01	0.01	0.06	0.04	0.04	0.03
	Cl	n.d.	n.d.	n.d.	n.d.	n.d.	n.d.
	F	1.75	0.46	3.02	0.97	3.02	0.97
	TOTAL	96.74	0.85	94.55	1.82	94.16	3.85
	F=O	0.73	0.19	1.28	0.41	1.27	0.41
site	cations (apfu)*						
M	Ca	9.59	0.10	9.37	0.33	9.41	0.37
	Na	0.03	0.02	0.06	0.02	0.05	0.13
	Sr	0.07	0.01	0.32	0.27	0.21	0.16
	Mn	n.d.	n.d.	0.01	0.02	0.01	0.01
	Fe	n.d.	n.d.	0.01	0.01	0.01	0.07
	Mg	0.01	0.02	0.05	0.10	0.05	0.17
	La	0.02	0.01	0.02	0.02	0.02	0.01
	Ce	0.03	0.03	0.04	0.04	0.04	0.04
	Pr	0.02	0.01	0.01	0.01	0.01	0.01
	Nd	0.01	0.01	0.01	0.02	0.01	0.02
T	P	5.89	0.11	5.70	0.54	5.74	0.61
	Si	n.d.	n.d.	0.04	0.02	0.03	0.01
X	F	0.94	0.24	1.63	0.58	1.64	0.56

n.d. = below detection limit, *atoms per formula units (apfu) calculated for 10 M-site atom occupancy.

Most of the trace-element concentrations detectable by LA-ICP-MS differ by two or three orders of magnitude. The chondrite-normalized distribution pattern of the rare earth elements (Fig. 2) presents a similar profile for the three varieties of apatite, with light rare earth elements — lanthanum (La) to neodymium (Nd) — enriched over the heavy ones — samarium (Sm) to lutetium (Lu). The chondrite-normalized lanthanum-ytterbium ratios (La/Yb_{cn}) ratios vary widely: for blue apatite, 194 to 799; for green apatite, 197 to 591; and for yellow apatite, 155 to 548. Chakmouradian et al. [3] found La/Yb_{cn} ratios between 30 and 500 for igneous apatite, and below 25 for hydrothermal varieties. All varieties of apatite in the siliceous carbonate ore found in Catalão are thus of igneous origin.

Conclusions

In this study, CL imaging identified three varieties of apatite that could be related to chemical signatures: (1) CL-blue apatite, probably primary, which presents few cationic and anionic site substitutions; (2) CL-green apatite, richer in strontium (Sr) and F, suggesting incipient carbonation, whose color may be attributed to higher manganese (Mn) values, occurring liberated or associated with blue apatite grains, especially at its rim, and (3) CL-yellow variety, whose mineral chemistry resembles the green type but presenting more inclusions and pores, also commonly assigning higher iron (Fe) values.

It is already known that the selectivity of flotation processes is significantly influenced by the specificity of the interactions between minerals and reagents;

therefore, variations in composition and the crystal structure of these minerals can change this phenomenon. The yellow apatite is impregnated with iron oxide-hydroxides and contains metal cations in the lattice, as seen in the microprobe results, which can affect the crystal lattice and crystallinity degree. This might further be the case for the minor and trace elements as assayed by LA-ICP-MS, which might vary in orders of magnitude. The presence of iron-bearing species on the mineral surface probably enhanced the hydrophilicity of apatite, resulting in the reduction of the adhesion of collector molecules onto the mineral surface sites. ■

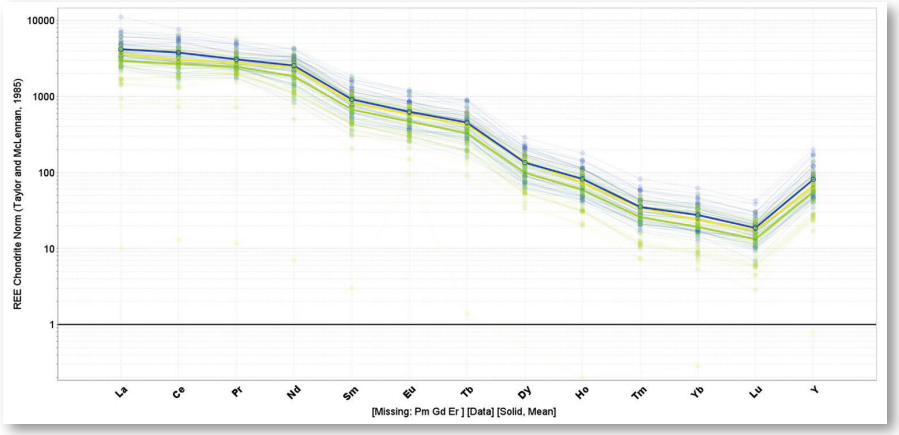

Fig. 2 Primitive-mantle-normalized spidergram showing relative concentrations of elements in apatite from Catalão. Primitive mantle data from Taylor and McLenman [4].

Selected references

1. Pufahl PK, Groat, LA (2017) Sedimentary and igneous phosphate deposits: formation and exploration. An invited paper. Economic Geology 112(3):483–516
2. Pasero M, Kampf AR, Ferraris C, Pekov IV, Rakovan J, White TJ (2010) Nomenclature of the apatite supergroup minerals. Eur J Mineral 22:163–179
3. Chakmouradian AR, Reguir EP, Zaitsev AN, Couëslan C, Xu C, Kynický J, Mumin AH, Yang P (2017) Apatite in carbonatitic rocks: compositional variation, zoning, element partitioning and petrogenetic significance. Lithos 274:188–213
4. Taylor SR, McClennan SM (1985) The continental crust: its composition and evolution. Blackwell, Oxford. 312 pp

Coal and rock classification with rib images and machine learning techniques

Yuting Xue
CDC NIOSH Pittsburgh Mining Research Division, Pittsburgh, PA, USA
*Corresponding author email: qcj1@cdc.gov

Full-text paper:
Mining, Metallurgy & Exploration (2022) 39:453–465, https://doi.org/10.1007/s42461-021-00526-4

Keywords: Rock classification, Image processing, Patch, Machine learning, SVM

Special Extended Abstract

The classification of rock and coal will assist in automated coal rib rating and shearer horizon control, and is studied with machine learning techniques in this work. A database of rock and coal images is created by filtering photographs taken by researchers from the National Institute for Occupational Safety and Health (NIOSH). The classifier was trained with patches extracted from the coal and rock images, and an accuracy score of 0.9 was obtained. The trained classifier was then applied to classify rock from a new coal rib image with three rock layers of different thicknesses, and good agreement was achieved. The results demonstrate that it is promising to use machine learning techniques and rib images for rock and coal classification.

Introduction

NIOSH researchers are currently developing a coal pillar rib rating (CPRR) technique to quantify the bearing capacity of coal ribs to eliminate injuries and fatalities due to rib falls [1]. The presence, location and thickness of rock partings affect the performance of coal ribs, and different adjustments are conducted for rib rating. Thus, one important step of coal rib rating is to classify rock from coal ribs. The classification of rock from coal ribs can also be applied for shearer horizon control at the longwall mining face. This enables a shearer to automatically track the interface between coal and rock, providing information for the shearer to adjust the cutting drum. In this work, machine learning techniques were applied to classify rock from coal rib images.

Database and method

Each image is made up of pixels. The pixel value represents the color intensity. For RGB images, there are three color channels: red, green and blue. An RGB image has three layers with each layer of a matrix of pixel values, and thus the image is represented as a three-dimensional array, which are features for machine learning.

The process to generate the databases is shown in Fig.1. During extensive field trips, NIOSH researchers took photographs to capture the failure mode of coal ribs. In order to capture the representative features of coal and rock, the photographs with fresh rock and/or coal surface were selected. Smaller images, or patches, were further extracted to

generate a large database. The patches have the same size of 50 × 50 in pixels and potentially contain the same amount of information for coal and rock, and the feature extraction and classification are conducted on the patches. There are 10,500 and 14,500 patches extracted for coal and rock, respectively, making a total of 25,000 patches for model training and validation.

Various machine learning techniques from the Scikit-Learn package were used [2]. Principal component analysis (PCA), a dimensionality reduction technique, was applied to extract meaningful features by projecting the data onto the principal axes and measuring the importance of each feature. The goal is to represent the data in a suitable lower dimension and retain essential features. Support vector machine (SVM) was used as the classifier. It is a discriminative classifier formally defined by a set of hyperplanes in a high- or infinite-dimensional space. The PCA preprocessor and SVM classifier could be further packaged into a pipeline. When there are new data, the pipeline preprocesses them and feeds the processed data into the classifier for prediction. Furthermore, a grid search cross-validation method was used to tune the model hyperparameters controlling the model performance. Finally, the database was randomly split into a training set (75 percent) to train the classifier, and a testing set (25 percent) to evaluate the model performance.

Results and discussions

Model performance. The performance of the trained SVM classifier was evaluated with the testing dataset. The evaluation shows there were 627 wrong predictions and 5,636 correct predictions, leading to an accuracy score of 0.900. At the same time, there were 295 false negative cases and 3,316 true positive cases, leading to a recall score of 0.918. The high accuracy score and recall scores demonstrate the capability of the classifier in classifying rock from coal.

Influence of patch size. Patch size affects the number of captured features, and different patch sizes, including 25 × 25, 50 × 50, 75 × 75 and 100 × 100 pixels, were used to study their influence on model accuracy. The learning curves, a tool to show how the model responds to increasing training data, show that the training and testing scores are converging to different values with increasing training data. The general trend is that larger patch size leads to higher testing score. However, the difference in testing scores decreases with increasing patch size. The testing curves for patch sizes of 75 × 75 and 100 × 100 almost overlap with any training size, indicating that, for the rock and coal image database, a size of 75 × 75 pixels is representative to include essential rock and coal features.

Application. A new rib image was used to show the application of the technique (Fig. 2). Part of the image with fresh surface was cropped and imported. A sliding window function was used to extract 50 × 50 patches from the input image. A total of 5,106 patches were extracted and fed into the pipeline for dimensionality reduction and prediction. The predicted rock patches are marked with a red border. It shows the approximate locations of the three rock layers. However, the accuracy depends on patch size and rock layer thickness. The top layer has the maximum thickness, and the whole layer is accurately predicted by overlapping patches. When the thickness reduces, there is less overlapped rock patches, resulting from the lesser contribution of the rock layer to the patch.

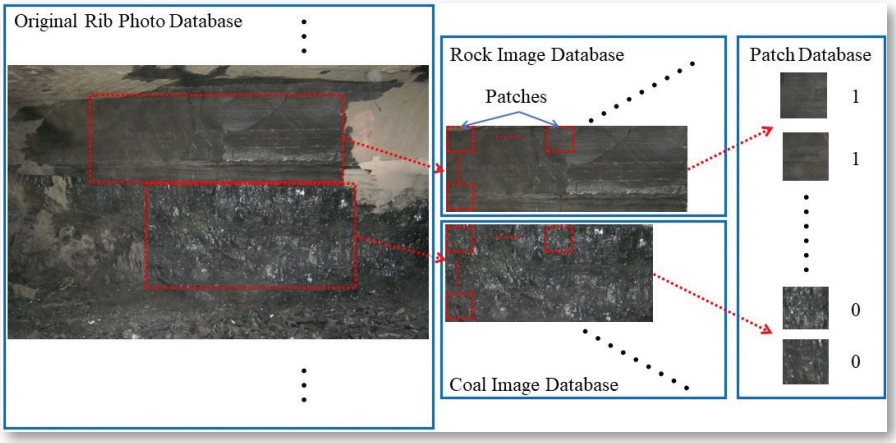

Fig. 1 Image-processing procedures to generate the database.

Conclusions

Machine learning techniques were used to classify rocks from coal rib images in gateroads. The trained SVM classifiers show good performance with an accuracy score of 0.90. It was then used to classify rock patches from a coal rib image. The highlighted rock patches illustrate the approximate location of the three rock layers. However, the accuracy depends on the rock layer thickness and patch size. ■

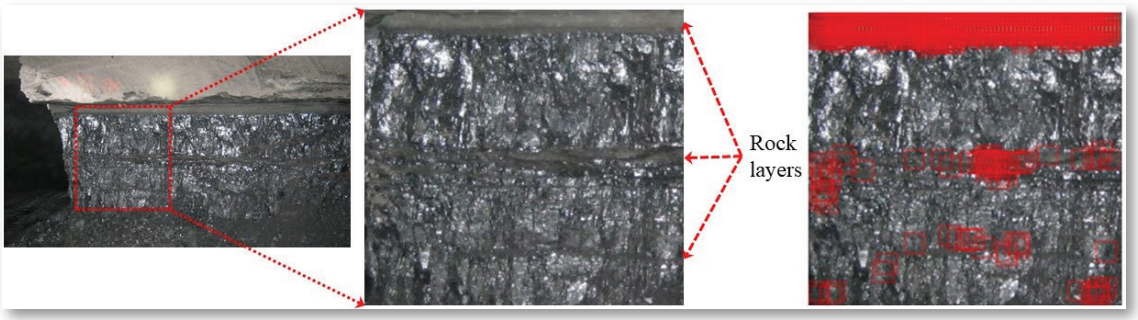

Fig. 2 Model application with SVM classifier.

Disclaimer

The findings and conclusions in this report are those of the author and do not necessarily represent the official position of the National Institute for Occupational Safety and Health, Centers for Disease Control and Prevention.

References

1. Mohamed KM, Xue Y, Rashed G, Kimutis R (2021) analyzing rib stability and support using a coal pillar rib rating. In the Proceedings of the 40th International Conference on Ground Control Mining, Canonsburg, PA, USA
2. Pedregosa F, Varoquaus G, Gramfort A, Michel V, Thirion B, Grisel O. Scikit-learn (2011) Machine learning in Python. J Mach Learn Res 12:2825–2830

Efficient separation and recovery of vanadium, titanium, iron and magnesium and synthesizing of anhydrite from steel slag

Jinrong Ju[1,2,3], Yali Feng[1,*], Haoran Li[2,3,*], Chenglong Xu[1] and Yi Yang[1]

[1]Civil and Resource Engineering School, University of Science and Technology Beijing, Beijing, China
[2]Key Laboratory of Biochemical Engineering, Institute of Process Engineering, Chinese Academy of Sciences, Beijing, China
[3]University of Chinese Academy of Sciences, Beijing, China
*Corresponding author emails: ylfeng126@126.com, hrli@ipe.ac.cn

Full-text paper:
Mining, Metallurgy & Exploration (2022) 39:733–748, https://doi.org/10.1007/s42461-022-00552-w

Keywords: Steel slag, Sulfuric acid leaching, Solvent extraction, Selective stripping, Oxalic acid precipitation

Special Extended Abstract

Steel slag is an industrial byproduct of steelmaking that is mainly composed of calcium, iron, silicon and magnesium. In addition, depending on the different raw materials entering the furnace, steel slag contains a certain amount of vanadium that is the main source of vanadium production, accounting for 69 percent of the species of the total vanadium raw material [1]. From experience, the production of one ton of steel will generate 1.0 to 1.5 tons of steel slag [2]. However, the utilization efficiency of steel slag is less than 30 percent, and a large amount of steel slag is identified as waste and stacked in tailings. The random stacking of steel slag not only wastes large amounts of limited steel and land resources but also exerts pressure on the environment [3], making it imperative to research the effective utilization of steel slag and recycling of metal resources.

Background

In the study, the process of leaching vanadium, titanium, iron and magnesium from steel slag and synthesizing of anhydrite at the same time is explored. The influences of acidity, temperature and time on metal leaching efficiency and slag phase composition are investigated. The separation process and mechanism of metals in the leaching solution are systematically studied, and the optimal separation conditions determined. The feasibility of recovering magnesium from solution to obtain magnesium oxide by oxalic acid precipitation method is researched, and the optimal conditions of precipitation explored.

Method

The steel slag used in the study was sourced from Pansteel & Iron Co. Ltd., located in the city of Panzhihua in Sichuan province in China. The leaching experiments of steel slag with sulfuric acid (H_2SO_4) solution were carried out with an electrically heated magnetic stirrer. After adding 100 mL of prepared H_2SO_4 solution of known concentration to a 250-mL Erlenmeyer flask and heating to the specified temperature, the steel slag was added while maintaining stirring. After the reaction was complete, a filtrate containing vanadium, titanium, iron and magnesium and leaching residue as calcium sulfate products were obtained by filtration.

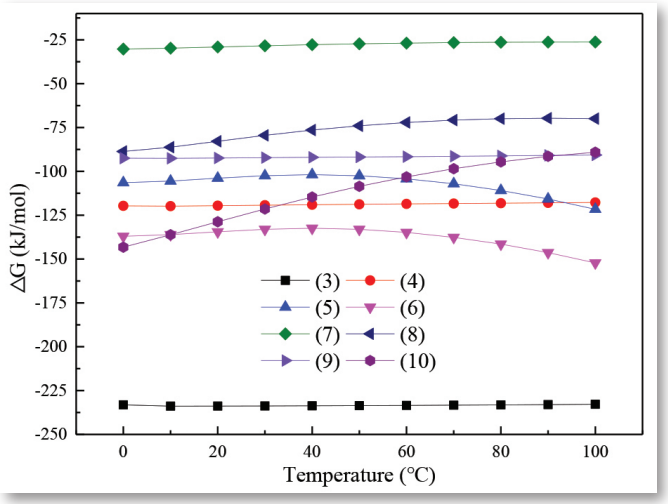

Fig. 1 Relationships between ΔG and temperature for the main reactions in the leaching process.

Results and discussion

The reactions of the compositions in steel slag with H_2SO_4 solution are given in Eqs. (1) to (8), and their thermodynamic diagrams are shown in Fig. 1.

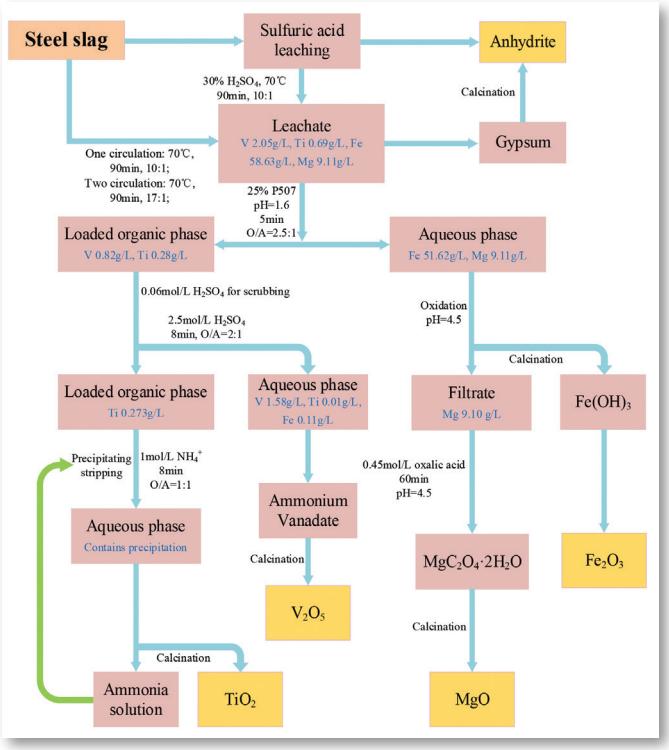

Fig. 2 Processing scheme for the recovery of vanadium, titanium, iron and magnesium and synthesizing anhydrite from steel slag.

$$2CaFe_2FeSi_2O_8(OH) + 9H_2SO_4 = 2CaSO_4 + 4FeSO_4 + Fe_2(SO4)_3 + 4H_2SiO_3\downarrow + 6H_2O \quad (1)$$

$$CaFe_3O_5 + 5H_2SO_4 = CaSO_4 + FeSO_4 + Fe2(SO_4)_3 + 5H_2O \quad (2)$$

$$Ca_2V_2O_7 + H_2SO_4 = (VO_2)_2SO_4 + 4CaSO_4 + H_2O \quad (3)$$

$$2Ca_2V_2O_7 + 8H_2SO_4 = 4VOSO_4 + O_2\uparrow + 4Ca_SO_4 + 8H_2O \quad (4)$$

$$FeO + H_2SO_4 = FeSO_4 + H_2O \quad (5)$$

$$Fe_2VO_4 + 3H_2SO_4 = 2FeSO_4 + VOSO_4 + 3H_2O \quad (6)$$

$$CaV_2O_5 + 3H_2SO_4 = CaSO_4 + 2VOSO_4 + 3H_2O \quad (7)$$

$$2V_2O_3 + O_2 + 4H_2SO_4 = 4VO_SO_4 + 4H_2O \quad (8)$$

It can be seen that the inherent crystal structure of the steel slag is destroyed by H_2SO_4 leaching, and the metal components such as vanadium and iron in the steel slag are converted into the corresponding sulfates and dissolved in the H_2SO_4 solution, while the calcium and silicon are converted into calcium sulfate precipitate and metasilicic acid as colloidal precipitate, respectively.

From the study, a scheme for the separation and recovery of vanadium, titanium, iron and magnesium and synthesizing of anhydrite from steel slag is proposed (Fig. 2).

First, the steel slag was leached with a 30 percent H_2SO_4 solution for 90 min at a leaching temperature of 70 °C and a liquid-solid ratio of 10:1 to obtain anhydrite with purity of 93.09 percent. The leachate can be recycled for the leaching of steel slag. The gypsum obtained in the cyclic leaching process was roasted at 200 °C to convert it into anhydrite. Finally, a leachate containing 2.05 g/L vanadium, 0.69 g/L titanium, 58.63 g/L iron and 9.11 g/L magnesium was obtained.

After the leachate was pretreated with sodium sulfite, the two-stage extraction efficiencies of vanadium and titanium were 99.45 and 99.98 percent, respectively, under the conditions of a P_50_7 concentration of 25 percent, organic-aqueous phase ratio (O/A) of 2.5:1 and aqueous pH of 1.6. The organic phase loaded with vanadium and titanium can be used to scrub iron with 0.06 mol/L H_2SO_4 solution. At an O/A of 2:1 and stripping time of 8 min, the single-stage stripping efficiency of vanadium was 93.78 percent with a 2.5 mol/L H_2SO_4 solution for the selective stripping of vanadium, while the stripping efficiency of titanium was only 1.30 percent, and 99.60 percent vanadium could be stripped through two-stage countercurrent stripping. The organic phase after stripping vanadium can be effectively stripped of titanium by using 0.8 mol/L ammonia solution.

Finally, through aeration treatment, the divalent iron in the raffinate was converted into trivalent iron. Adjusting the pH to 5.0 can convert almost all iron (99.86 percent) into $Fe(OH)_3$. At a dosage of oxalic acid of 0.45 mol/L, pH of 5.5, precipitation time of two hours and precipitation temperature of 25 °C, 98.39 percent of the magnesium in the solution can be converted into magnesium oxalate dihydrate precipitation.

Conclusion

In this work, an approach for the efficient separation and recovery of vanadium, titanium, iron and magnesium and synthesizing of anhydrite from steel slag is investigated. Steel slag can be directly leached by H_2SO_4 solution under normal pressure to get a leachate rich in vanadium, titanium, iron and magnesium as well as an anhydrite solid phase product with purity of 93.09 percent. Under the conditions of a P_50_7 concentration of 25 percent and aqueous pH of 1.6, through two-stage countercurrent extraction, the extraction efficiency of vanadium and titanium were 99.45 and 99.98 percent, respectively. The single-stage stripping efficiency of vanadium was 93.78 percent with 2.5 mol/L H_2SO_4 solution. The single-stage stripping efficiency of titanium was 99.73 percent with 0.8 mol/L ammonia solution. Vanadium and titanium in the organic phase can be selectively stripped by H_2SO_4 and ammonia solution, respectively. The solution after precipitation of iron can be used to effectively recover the magnesium resources in the solution by oxalic acid precipitation.

This process not only recovers resources such as vanadium, titanium, iron and magnesium in steel slag but also converts calcium into anhydrite to be recovered, providing a new avenue for the comprehensive utilization of steel slag. ■

References

1. Lee J-C, Kurniawan E-yK, Chung KW, Kim R, Jeon H-S (2021) Review on the metallurgical recycling of vanadium from slags: towards a sustainable vanadium production. J Market Res 12:343–364
2. Das P, Upadhyay S, Dubey S, Singh KK (2021) Waste to wealth: recovery of value-added products from steel slag. J Environ Chem Eng 9(4):105640
3. Xiao B, Wen Z, Miao S, Gao Q (2021) Utilization of steel slag for cemented tailings backfill: hydration, strength, pore structure, and cost analysis. Case Stud Constr Mater 15:e00621

A comprehensive roof bolter drilling control algorithm for enhancing energy efficiency and reducing respirable dust

Hua Jiang[1,*] and Yi Luo[2]

[1]National Institute for Occupational Safety and Health (NIOSH), Centers for Disease Control and Prevention (CDC), Pittsburgh, PA, USA
[2]Department of Mining Engineering, West Virginia University, Morgantown, WV, USA
*Corresponding author email: hujiang@mix.wvu.edu

Full-text paper:
Mining, Metallurgy & Exploration (2022) 39:241–249, https://doi.org/10.1007/s42461-022-00566-4

Keywords: Roof bolter, Drilling control, Respirable dust, Specific energy, Bit condition

Special Extended Abstract

A roof bolting drilling operation in an underground coal mine can expose the operator to a high concentration of respirable coal and crystalline silica dusts (smaller than 10 µm). Overexposure of high-level quartz dust for a roof bolter operator can lead to the development of silicosis in as little as three years [1]. This study proposes a drilling control algorithm for the bolt hole drilling process. This algorithm can be integrated into a current drilling control system on the roof bolter machinery and is expected to reduce the generation of respirable dust while enhancing the energy efficiency of the roof bolter machine. In addition, the drilling efficiency and bit condition can be evaluated while drilling based on the real-time feedback parameters. This capability enables the algorithm to ensure the drilling is performed under a relatively high energy efficiency with less respirable dust generation and to avoid drilling with an excessively worn bit that can cause bit clogging or steel buckling failure.

Background

Investigations on the respirable coal and quartz dust hazards that occurred during an underground roof bolting cycle were conducted by researchers [2]. The results indicate a quartz content of more than 50 percent can be found from the total roof bolting dust. For the sub-5 µm fraction, the quartz content can be as much as 20 percent. These quantified results confirmed that roof bolting dust contains a higher percentage of quartz than other dust sources from mining activities. Several dust control technologies, such as vacuum dust collection systems and canopy air curtains, have been developed and implemented to address the exposure issue for the roof bolter operator [3]. The research in this study is focused on investigating the relationship of drilling control parameters, such as penetration and rotation rates and bit condition, with the dust generation characteristics, then proposing a drilling control algorithm to minimize the respirable dust generation while increasing the drilling energy efficiency.

Method

Fifty-two laboratory drilling tests were conducted on a Fletcher drilling test platform. Dust samples from the dust collection system were collected and analyzed in the laboratory for their size distributions.

In this study, drilling bite depth, b, defined as bit penetration depth per revolution, was introduced to describe the roof bolter drilling process. Drilling bite depth can be calculated from penetration, v, and rotational rate, w, with the following equation:

$$b = \frac{60v}{w} \quad (1)$$

The specific energy is used for evaluating the energy efficiency of the roof bolter machine in this study. The specific energy for rotary drilling can be expressed mathematically in terms of drilling bite depth, penetration rate, torque and thrust, as shown in [4]:

$$\varepsilon = \frac{2\pi T}{A_b \cdot b} + \frac{W}{A_b} \quad (2)$$

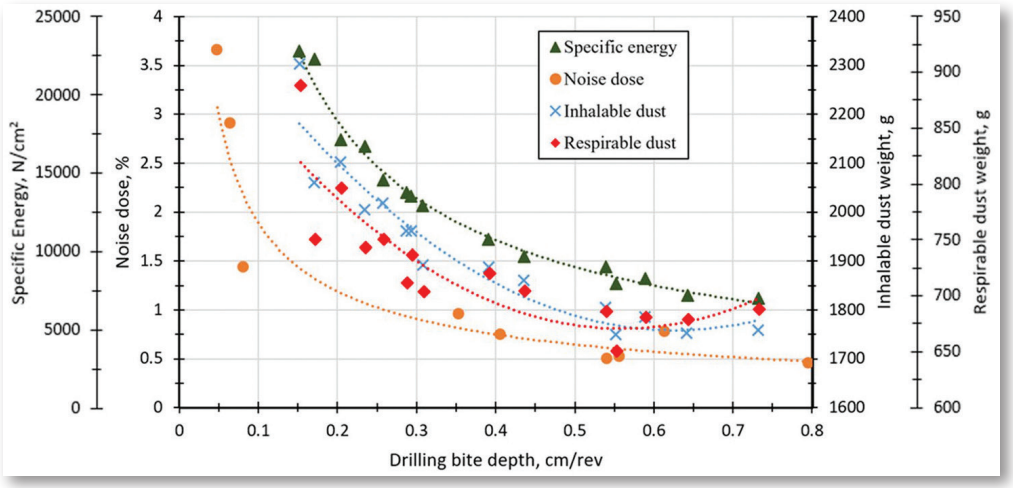

Fig. 1 Relationships of drilling bite depth with noise dose, dust weight and specific energy.

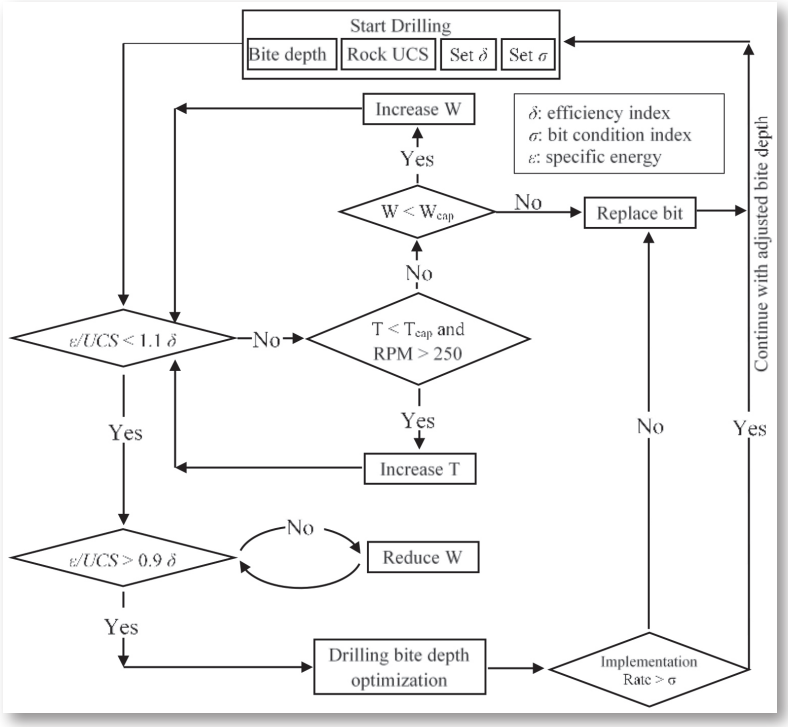

Fig. 2 Schematic diagram of the drilling control algorithm.

where A_b is the borehole area in cm^2, b is the drilling bite depth in cm/rev, and T and W are the torque and thrust in Nm and N, respectively. It should be noted that all these parameters were monitored and recorded in real time by the drilling control system.

Results

The concrete drilling inhalable and respirable dust weight, specific energy, and noise dose results are plotted against the achieved bite depth in Fig. 1. It was shown that specific energy reduced significantly while drilling with a larger bite depth, which also indicates improved energy efficiency with higher bite depth. A 70 percent reduction was achieved when increasing the bite depth from 0.152 to 0.732 cm/rev. Both inhalable and respirable dust weight results show a rapid decrease as bite depth increases, until bite depth reaches 0.541 cm/rev. However, after this point, the generation rate of inhalable dust becomes stable with further increase of bite depth. Meanwhile, the respirable dust shows an uptick after this point in the operation. Overall, the generated inhalable and respirable dust are reduced by 550 and 200 g, respectively, within the tested drilling bite depth range.

Discussion and conclusion

As stated, the optimum bite depth is the depth when the specific energy reaches the minimum. However, it is impractical to achieve the optimum bite depth due to safety and power limitations. A rational bite depth is that for which any further increase in bite depth will only result in an insignificant reduction in drilling specific energy.

The recommended drilling control algorithm is shown in Fig. 2. In a real-time drilling process, the drilling acquired — that is, penetration and rotational rates, thrust and torque — are used with bite design and wear condition to determine rock strengths. The rock strength is then used to determine the rational bite depth. Because a higher rotation rate, RPM, would accelerate bit wear, a lower RPM combined with a correlated rate of penetration, ROP, is preferable to reach a targeted drilling bite depth. In addition, an excessively worn drill bit prevents the system from achieving the targeted bite depth and can increase the respirable and inhalable dust generation rates by as much as 61.5 percent (respirable) and 43.6 percent (inhalable). The overall drilling specific energy using a worn bit is higher than a new bit due to the increased rubbing area and friction between the drill bit and the rock. Therefore, a bit wear condition check is included in the algorithm according to the implementation rate (achieved versus targeted bite depth). When the drill penetrates a different rock layer with its determined strength significantly different from the previous layer, a rational bite depth is determined based on the rock unconfined compressive strength, UCS, bit wear condition, and implementation rate. As the drilling progresses, the specific energy is monitored, and the ratio can be calculated simultaneously. If the ratio is within 10 percent of the efficiency index, then the system will continue drilling with the initial bite depth. However, the algorithm still needs to evaluate the bit condition using the implementation rate. If the implementation rate is lower than the bit condition index, the system will stop, and a new bit needs to be installed to continue drilling.

By adapting this drilling control algorithm, the drilling efficiency and bit condition can be monitored in real time, so that at any point in the drilling the system can stay in a relatively high energy efficiency with less respirable dust production and also reduce the chance to encounter bit clogging or steel buckling, which can expose the operator to a tremendous safety and health hazard. Due to the limitation of the data sources, to improve the algorithm's prediction accuracy for respirable dust and noise production rates, more dust and noise results from drilling different types of rock need to be collected for the calibration process. ■

References

1. MSHA (2014) Exposure to Coal Mine Dust Containing Quartz, Health Hazard Information Card HH-47. U.S. Department of Labor, Mine Safety and Health Administration
2. Joy GJ, Beck TW, Listak JM (2010) Respirable quartz hazards associated with coal mine roof bolter dust. Proceedings of the 13th U.S./North American Mine Ventilation Symposium, pp. 59–64
3. Reed WR, Klima S, Shahan M, Ross GJH, Singh K, Cross R, Grounds T (2019) A field study of a roof bolter canopy air curtain (2nd generation) for respirable coal mine dust control. Int J Min Sci Technol
4. Jiang H, Luo Y, Yang J (2018) The mechanics of bolt drilling and theoretical analysis of drilling parameter effects on respirable dust generation. J Occup Environ Hyg 15(9):700–713